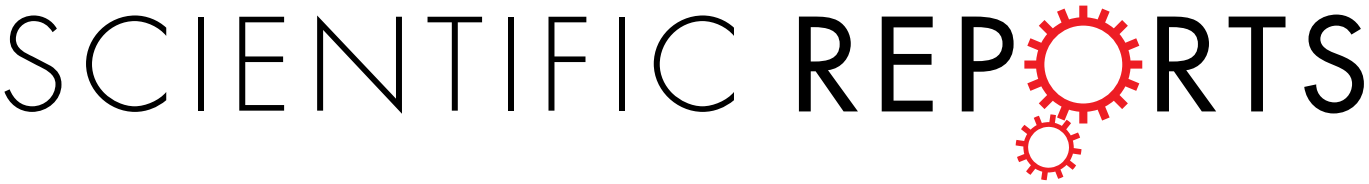

OPEN

Coherent Nonlinear Optical Response Spatial Self-Phase Modulation in $MoSe_2$ Nano-Sheets

Received: 10 September 2015
Accepted: 05 February 2016
Published: 26 February 2016

Wenhui Wang[1], Yanling Wu[2], Qiong Wu[2], Jiaojiao Hua[1] & Jimin Zhao[2]

Two-dimensional (2D) transition metal dichalcogenides (TMDs) are drawing increasing interest due to their relatively high carrier mobilities, valley pseudospins, and gapped electronic structures, which all indicate interesting nonlinear optical properties of these 2D materials. However, such nonlinear optical properties are so far less investigated and their correlation with the electronic structure of the material is rarely probed. In this work, we have systematically investigated the spatial self-phase modulation (SSPM) of $MoSe_2$ flakes in a suspension form, which is a coherent third-order nonlinear optical effect. The nonlinear susceptibility $\chi^{(3)}$ and its wavelength-dependence are measured, yielding a value of 1.1×10^{-9} e.s.u. (SI: 1.53×10^{-17} m^2/V^2) at 532 nm laser excitation for effective one-layer $MoSe_2$.

The discovery of graphene has aroused tremendous interest in two-dimensional (2D) materials. Layered transition metal dichalcogenides (TMDs) are drawing increasing interest owing to their high carrier mobilities[1–4] and semiconducting properties. For TMDs such as MoS_2, $MoSe_2$ and WTe_2, a dramatic change occurs from an indirect bandgap in the bulk to a direct bandgap in the monolayer limit[5]. Moreover, these layered materials exhibit metallic, semiconducting or superconducting properties, depending on the coordination and oxidation states of the metal atoms. In addition, large effects of excitons[6], strong photoluminescence[5,7,8] and fully optical control of charge carriers in the valleys[6,9,10] endow them with a wide range of applications in optoelectronics and valleytronics[7,11–15]. Besides the aforementioned electronic and linear optical properties, nonlinear optical properties of these novel quantum materials[16–23] have also been investigated, which can enrich the comprehensive understanding of the behavior of carriers in 2D materials and extend solid basis for the potential optoelectronic applications[24–31]. Significantly, it has been demonstrated that SSPM provides a way to induce non-local ac electron coherence in the TMDs[16] and measure their nonlinear optical susceptibilities. Here we carry out a parallel investigation on another TMD, $MoSe_2$, to measure its wavelength-dependent $\chi^{(3)}$.

Investigating the nonlinear optical properties of these novel materials is quite essential since, if the optical properties of these newly discovered quantum materials are superb, it will for the first time make it possible to integrate electronic and optoelectronic devices in one material system, which is so far challenging to realize in the indirect-gap silicon and no-gap graphene systems. Among such optical properties, nonlinear optical properties are even more critical, because, besides lasing itself, most of the photonics applications are based on nonlinear optical properties[32–36]. For example, optical switches, which are as important to photonics as transistors to electronics, are all realized using various nonlinear optical effects (*e.g.,* four-wave mixing[37], three-wave mixing[38], SSPM[16], *etc.*)—the switching itself can only be a nonlinear process. In terms of nonlinear optical processes, the second harmonic generation only occurs in materials without inversion symmetry (*i.e.,* limited materials, most of which cannot be integrated)[39], and the forth-order and higher-order nonlinear optical effects are usually much weaker than the third-order responses. Therefore it is essential to obtain the knowledge about the third-order nonlinearity $\chi^{(3)}$[16,17,24,40–43]. Knowing its magnitude and dependence on the working wavelength is very useful in selecting the materials and designing an optoelectronic device.

Spatial self-phase modulation, which was initially investigated in nematic liquid crystal in 1981[44], is a purely coherent nonlinear optical effect that is characterized by an intensity-dependent refractive index $n = n_0 + n_2 I$, where n_0 and n_2 are linear and nonlinear refractive indices and I is the laser intensity. The effect is also known as optical Kerr effect, which can induce self-focusing in the crystal or other type of materials when the effect is strong enough. The SSPM is a third-order nonlinear optical process (parallel to that of third harmonic generation and four-wave mixing), which is characterized by an additional transverse wavevector developed due to the

[1]School of Science, Xi'an Jiaotong University, Xi'an 710049, China. [2]Beijing National Laboratory for Condensed Matter Physics and Institute of Physics, Chinese Academy of Sciences, Beijing 100190, China. Correspondence and requests for materials should be addressed to J.Z. (email: jmzhao@iphy.ac.cn)

transverse gradient in refractive index. When passing through the sample, the optical phase of incident beam depends on the transverse light intensity distribution, resulting in a conical out-going diffraction and interference in the far field (as the concentric fringes). As a result, the outgoing beams do not propagate along the incidence direction anymore. The rings are prominently different from the well-known Newton's ring (a linear optics phenomenon) in that the ring number N in SSPM is finite and linearly dependent on the laser fluence. In addition, the outermost ring is the thickest among all the concentric fringes. In SSPM investigations, N directly reflects the optical phase (*i.e.*, the exact nonlinear effect as reflected by n_2 and $\chi^{(3)}$) and is correlated to the electronic phase and coherence of the material[16]. Thus it is a more essential and intrinsic observable than the ring diameter D, because D can also be modified by the linear refractive index n_0.

Unlike other nonlinear optical effects, the effect of SSPM can be observed conveniently by using both continuous wave (cw) and ultrafast lasers with only milliwatts laser powers. Furthermore, the nonlinear refractive index n_2, hence the third-order nonlinear susceptibility $\chi^{(3)}$, can be directly and quantitatively obtained through a convenient way[16,17]. Therefore, this experimental method has been developed to be a general way for measuring the $\chi^{(3)}$ of 2D layered quantum materials[16,17]. It applies to the broad spectrum-regime including the violet and ultra-violet regime, where third harmonic generation and four-wave mixing are ineffective. It can also be applied to the situation when large single crystal is hard to achieve. Significantly, since a wind-chime model[16] has been developed to account for the emergence of ac electron coherence in the materials, this method has endowed the capability of comparing and correlating to the electronic band structure of a specific layered quantum material.

In this work, we directly measured the wavelength-dependent coherent nonlinear optical response SSPM of nanoscale $MoSe_2$ sheets, and obtained their $\chi^{(3)}(\omega)$ values. Comparison with absorption has been carried out, further demonstrating SSPM as a useful method in probing the electronic band structure of layered materials.

Results and Discussion

Linearly polarized cw laser beams with various wavelengths have been employed to excite the $MoSe_2$ suspension (*Methods and Materials*). The schematics of our experimental setup is shown in Fig. S1 (*see supporting information*). The interaction between the incident light and the $MoSe_2$ flakes is schematically illustrated in Fig. 1a, where the red honeycomb lattices represent the $MoSe_2$ flakes. As a result of the interaction, these flakes are rotated and aligned to be along the light polarization direction. A typical scanning electron microscope (SEM) image of the $MoSe_2$ flakes is shown in Fig. 1b, where the dimension of most of the flakes is about 0.3~2 μm. As shown, most of the $MoSe_2$ flakes in our experiment are multi-layered bulk materials. In Fig. 1(c–e) we show typical SSPM diffraction ring patterns for the 735 nm, 532 nm and 473 nm excitations, respectively, which are concentric rings resulted from the conical out-coming beams. Note that the outermost ring is thickest and has the strongest intensity, with those of others decrease towards the center. The calculation result of the radial intensity distribution is shown in Fig. S2 (*see supporting information*). It can be seen that the calculation result compares well with the experimental observation shown in Fig. 1d. For each laser wavelength, the ring pattern is clear and uniform. The fringes have sharp edges, and their thicknesses become narrower when the laser beam covers more number of the flakes[16]. To make sure that the concentric diffraction rings are not resulted from the solution itself, we have carried out a control experiment where the pure suspension without any $MoSe_2$ flakes was used. It can be seen in Fig. S3 (*see supporting information*) that no diffraction rings can be observed on the white screen at the far field when a 532 nm laser beam was introduced, even though the laser power is increased to our laser's maximum output 355 mW.

To focus on the pattern formation process, we show the snapshots of the emergence of the SSPM rings in Fig. 2. It can be seen that the number of rings increases steadily with time until the maximum is reached after around 0.3~0.5 s. This temporal evolution of the pattern formation is well explained by our recently proposed wind-chime model[16]. Taking the model, the 0.4 s time duration is the time interval needed for the rotation and alignment of the flakes by the incident light—the emergence of the electron coherence and its maximization. The electrons at excited state are forced to oscillate at the excitation optical frequency, which further emit light to form the diffraction rings at the far field. Without the presence of a laser beam, each $MoSe_2$ flake suspended in the solution can be treated as an independent domain, whose orientation is arbitrary. Thus, the phases of the electronic wave functions[16] of the photo-induced charge carriers or holes or excitons in each domain are completely irrelevant. However, when a polarized laser beam is applied, each flake will get aligned in a way that they have an axis parallel to the light polarization. This aligning process is achieved due to the energy relaxation. When the $MoSe_2$ flakes are fully aligned, the photon-induced carriers in each domain experience reduced boundary scattering, leading to less stray lights in the diffraction. Therefore, this SSPM process becomes a nearly purely coherent nonlinear optical process. Other than this purely coherent factor, the reduction of the refractive index heterogeneity also leads to enhanced coherence, because the light absorption, carrier mobility and effective mass are different along x, y and z axes.

The subsequent deformation (not shown in Fig. 2, but can be seen in Fig. 1c–e) can be attributed to a thermal effect, where the density of the solution becomes asymmetric under laser heating and gravitation[17,45]— the linear index n_0 is modified to be non-uniform along the vertical direction. During this latter process, n_2 and $\chi^{(3)}$ do not change since the number of rings N remains unchanged. It is worth noting that there is so far no direct experimental observation of a thermal gradient ΔT for the initial ring formation process (Fig. 2), although ΔT is frequently assumed as the starting point in many theoretical simulations. Note that this is quite different from the situation for the latter ring deformation process (Fig. 1c–e). In our experiment, the rings all develop to full circle till the maximum number of rings is reached. No pattern deformation occurs during the increase of the ring number (Fig. 2). Since the initial pattern formation process is clearly seperated from the next (following) pattern deformation process, thermal effect does not contribute to the initial pattern formation process (Fig. 2). Thermal effect only contributes to the latter (following) pattern deformation process. Most of the laser heat is dissipated (in the deformation process) through transfering to the solution and ultimately gone by evaporization.

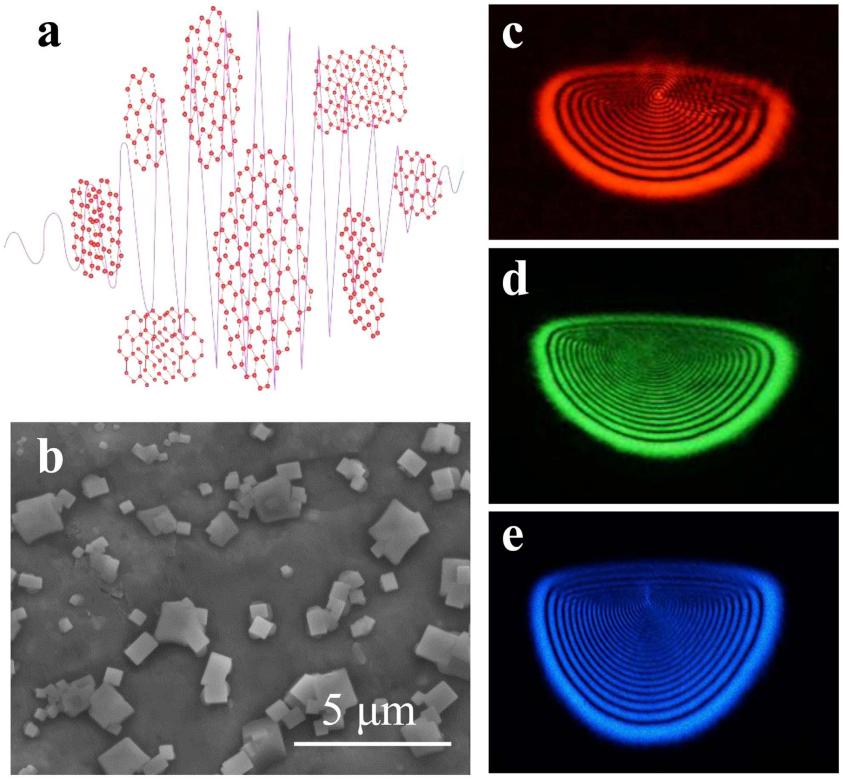

Figure 1. (**a**) Schematic illustration of the interaction between incident light and the $MoSe_2$ flakes. (**b**) A SEM image of the $MoSe_2$ flakes. (**c**–**e**) Typical SSPM patterns generated from the $MoSe_2$ suspension under laser excitations with wavelengths of 735 nm, 532 nm, and 473 nm, respectively.

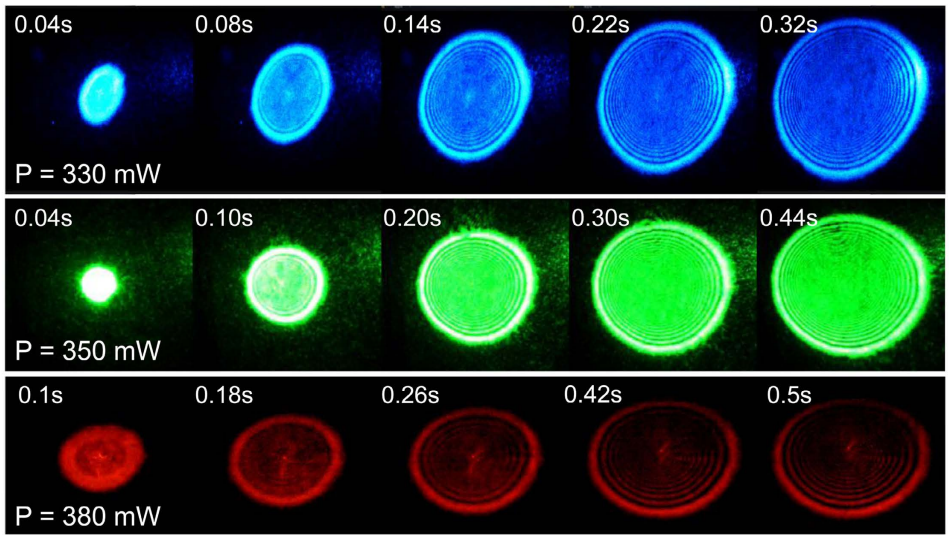

Figure 2. Snapshots of the SSPM ring pattern formation process under laser excitations with wavelengths of 735 nm, 532 nm, and 473 nm, respectively. The whole formation process takes 0.3~0.5 s.

The intensity dependence of the ring number N for different wavelengths are shown in Fig. 3. It can be seen that N increases nearly linearly with the laser beam intensity I and the slops of the data vary with the laser wavelength (*i.e.*, the excitation photon energy). Consequently, the values of n_2 can be directly obtained from the slopes in Fig. 3 with $n_2 = (\lambda/2n_0L)(N/I)$, where L is the thickness of $MoSe_2$ suspension. Taking $L = 10$ mm, $n_0 = 1.47$, we acquire that $n_2 = 3.24 \times 10^{-10}$ m^2/W for a 532 nm laser beam. Based on the one-to-one correspondence, the magnitude of the third-order nonlinear susceptibility can be obtained according to the relation[16,17]

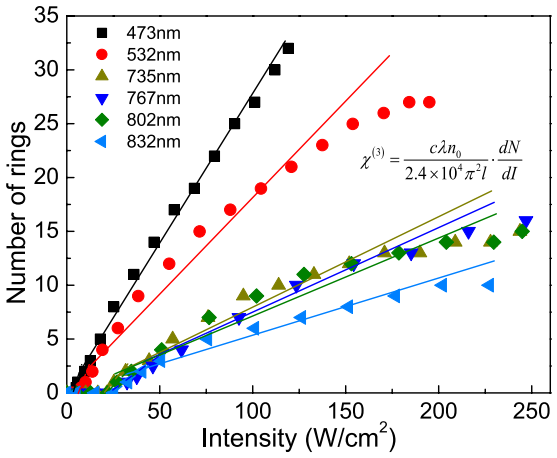

Figure 3. Dependence of the ring number *N* on incident laser intensity *I* for different wavelengths. The solid lines are guides to the eye for the overall linear relation and the corresponding slopes directly yield the third-order nonlinear optical susceptibility $\chi^{(3)}$ for different wavelengths.

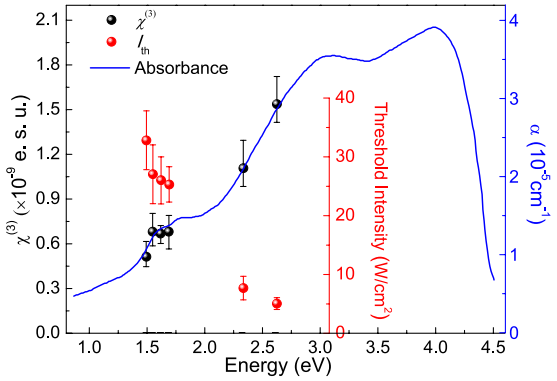

Figure 4. Comprehensive illustration of the $\chi^{(3)}$ (black dots) and intensity threshold I_{th} (red dots) for the near-infrared to visible spectral range. The blue solid curve is adopted from ref. 34 and illustrates the absorption spectrum for a sputtered $MoSe_2$ thin film. The well comparison between the $\chi^{(3)}$ data with the absorption curve shows their proportionality.

$n_2 = (12\pi^2/nc)10^3\chi^{(3)}$, which yields a value of 1.8×10^{-4} (e.s.u.). The value of $\chi^{(3)}$ for effective one-layer $MoSe_2$ can be estimated from $\chi^{(3)}_{total} = M^2\,\chi^{(3)}_{one\text{-}layer}$, where M is the effective number of $MoSe_2$ layer that the laser beam traverses through. By estimating M to be around 400 in our experiment [*Methods and Materials*], we obtain that the value of $\chi^{(3)}$ for effective one-layer $MoSe_2$ is about 1.1×10^{-9} e.s.u.

We further investigated the wavelength dependence of the SSPM effect. The $\chi^{(3)}$ and intensity thresholds at various wavelengths have been measured and shown in Fig. 4, respectively. It can be seen that $\chi^{(3)}$ increases steadily with decreasing wavelength. Significantly, its value is well proportional to the light absorption measured by J. Pouzet *et al.* for sputtered $MoSe_2$ layers[46]. The correlation between $\chi^{(3)}$ and absorption demonstrates that $\chi^{(3)}$ is determined by the band structure. In the photo-generation of free carriers or excitons, the quantum transition probability is proportional to the occupation number of the valance and conduction bands. The integration of such transition probabilities in the momentum space yields a value that is proportion to the $\chi^{(3)}$ value we measured here. Therefore, our current experiment further demonstrates that SSPM can be an effective method to probe the integrated information of the electronic band structure of a layered material. It can be used to experimentally verify whether the theoretical calculation of the band structure is correct—as absorption spectroscopy can do. And the wavelength-dependence of $\chi^{(3)}$ is sensitive to different layered materials, which can certainly be useful in characterizing new materials in the future. Here, at relatively higher photon energies, some of the in-active transitions become accessible; thus the value of $\chi^{(3)}$ is higher for higher photon energies and the value of threshold is lower for higher photon energies, correspondingly (Fig. 4).

During the above process, the outermost ring thickness and the ring diameter also show linear dependences on I, ending by the frequently observed thermal effect causing a "half-ring"[17,45]. As discussed above, D can be directly affected by not only n_2 but also n_0, thus a less important observable. However, the linear dependence of D on I makes the SSPM effect practical for all-optical switching[16], particularly with that a weak beam can control a strong beam with high contrast ratio[16,38]. The TMD materials can be integrated and tailored, and the switches can

be cascaded. Thus our nonlinear optical investigation here further demonstrates the great potential for TMDs in ultrafast photonics applications.

In conclusion, we have unambiguously observed the nonlinear optical response SSPM in a suspension of $MoSe_2$ flakes, yielding a value of 1.1×10^{-9} e.s.u. (*i.e.*, $1.53 \times 10^{-17}\,m^2/V^2$) for the nonlinear dielectric susceptibility $\chi^{(3)}$ for an effective one-layer at 532 nm excitation. The wavelength-dependence $\chi^{(3)} = \chi^{(3)}(\omega)$ was measured for $MoSe_2$, which is proportional to that of the light absorption. This confirms that SSPM is a ubiquitous property of a layered quantum material, which can be well described by the wind-chime model we previously developed[16]. Our investigation further demonstrates application potentials of $MoSe_2$ and other TMDs in photonics, such as all-optical switching and optical limiting.

Methods and Materials

The sample preparation is similar to that in Ref. [16] for MoS_2. Micrometer-sized $MoSe_2$ powder (LSKYD, http://www.kydmaterials.com/en/index.php) was added into a N-methyl-2-pyrrolidinone (NMP) solvent, followed by 30 minutes of ultrasonication. The $MoSe_2$ flakes are uniformly distributed and suspended in the solution without observable aggregation. The density (C) of $MoSe_2$ is 7.1×10^{-4} mol/L. In the experiment, linearly polarized cw laser beams with various wavelengths (473 nm, 532 nm 735 nm, 767 nm, 802 nm and 832 nm) were focused onto the $MoSe_2$ suspension using a lens of 200 mm focal length. The illuminated area in the suspension is estimated to be 0.182 mm^2 with a $1/e^2$ intensity radius of 0.24 mm. The light at the out-coming surface is diffracted off the initial propagation direction. At propagating to the far field, they interfere with each other to form conical output beams, which produce sharp concentric fringes on the white screen.

The number of effective layers of the $MoSe_2$ flakes that the laser beam passes through can be estimated as follows. The volume of the solution (V) is 4×10^{-3} L. The total number of ($MoSe_2$) molecules in the solution is $C \times V \times N_A$ ($=1.71 \times 10^{18}$), where N_A is the Avogadro's number. Meanwhile, since the area of the cross-section of the cuvette is S ($=1\,cm \times 4\,cm$), the total number of molecules in one effective layer is S/a^2, where a ($=3.299$ Å) is the lattice constant of $MoSe_2$. Thus, the number of effective layers can be obtained as $C \times V \times N_A / (S/a^2) = 403 \approx 400$.

When we use SSPM to measure $\chi^{(3)}(\omega)$, it is necessary to make sure the saturation due to sample concentration will not occur and the sample itself is very stable during the measurement. To do so, it is suggested to make sure that the sample concentration is relatively low such that there is no precipitation of flakes and it is as low as being able to measure the fringe numbers conveniently.

References

1. Novoselov, K. S. *et al.* Two-dimensional atomic crystals. *Proc. Natl. Acad. Sci. USA* **102,** 10451–10453 (2005).
2. Jiang, Y. J., Low, T., Chang, K., Katsnelson, M. I. & Guinea, F. Generation of pure bulk valley current in graphene. *Phys. Rev. Lett.* **110,** 046601 (2013).
3. Zhang, F., Jung, J., Fiete, G. A., Niu, Q. A. & MacDonald, A. H. Spontaneous quantum Hall states in chirally stacked few-layer graphene systems. *Phys. Rev. Lett.* **106,** 156801 (2011).
4. Bahniman, G. & Naval, K. An ab initio study of strained two-dimensional $MoSe_2$. *J. Semicond.* **36,** 043001–043005 (2015).
5. Tongay, S. *et al.* Thermally driven crossover from indirect toward direct bandgap in 2D Semiconductors: $MoSe_2$ versus MoS_2. *Nano Lett.* **12,** 5576–5580 (2012).
6. Debbichi, L., Eriksson, O. & Lebegue, S. Electronic structure of two-dimensional transition metal dichalcogenide bilayers from ab initio theory. *Phys. Rev. B* **89,** 205311 (2014).
7. Zhang, Y. *et al.* Direct observation of the transition from indirect to direct bandgap in atomically thin epitaxial $MoSe_2$. *Nat. Nanotech.* **9,** 111–115 (2014).
8. Tonndorf, P. *et al.* Photoluminescence emission and Raman response of monolayer MoS_2, $MoSe_2$, and WSe_2. *Opt. Express* **21,** 4908–4916 (2013).
9. Xu, X. D., Yao, W., Xiao, D. & Heinz, T. F. Spin and pseudospins in layered transition metal dichalcogenides. *Nat. Phys.* **10,** 343–350 (2014).
10. Mak, K. F., Lee, C., Hone, J., Shan, J. & Heinz, T. F. Atomically Thin MoS_2: A new direct-gap semiconductor. *Phys. Rev. Lett.* **105,** 136805 (2010).
11. Xiao, D., Yao, W. & Niu, Q. Valley-contrasting physics in graphene: Magnetic moment and topological transport. *Phys. Rev. Lett.* **99,** 236809 (2007).
12. Mak, K. F., He, K. L., Shan, J. & Heinz, T. F. Control of valley polarization in monolayer MoS_2 by optical helicity. *Nat. Nanotech.* **7,** 494–498 (2012).
13. Zhao, W. J. *et al.* Evolution of Electronic electronic structure in atomically thin sheets of WS_2 and WSe_2. *ACS Nano* **7,** 791–797 (2013).
14. Jones, A. M. *et al.* Optical generation of excitonic valley coherence in monolayer WSe_2. *Nat. Nanotech.* **8,** 634–638 (2013).
15. Ramasubramaniam, A. Large excitonic effects in monolayers of molybdenum and tungsten dichalcogenides. *Phys. Rev. B* **86,** 115409 (2012).
16. Wu, Y. L. *et al.* Emergence of electron coherence and two-color all-optical switching in MoS_2 based on Spatial Self-Phase Modulation. *Proc. Natl. Acad. Sci. USA* **112**(**38**), 11800–11805 (2015).
17. Wu, R. *et al.* Purely coherent nonlinear optical response in solution dispersions of graphene sheets. *Nano Lett.* **11,** 5159–5164 (2011).
18. Cheng, J. L., Vermeulen, N. & Sipe, J. E. Third-order nonlinearity of graphene: Effects of phenomenological relaxation and finite temperature. *Phys. Rev. B* **91,** 235320 (2015); Cheng, J. L., Vermeulen, N. & Sipe, J. E. Third order optical nonlinear of graphene. *New J. Phys.* **16**, 053014 (2014).
19. Hendry, E. *et al.* Coherent nonlinear optical response of graphene. *Phys. Rev. Lett.* **105,** 097401 (2010).
20. Yin, X. *et al.* Edge nonlinear optics on a MoS_2 atomic monolayer. *Science* **344,** 488–490 (2014).
21. Janisch, C. *et al.* Extraordinary Second Harmonic Generation in tungsten disulfide monolayers. *Sci. Rep.* **4,** 5530 (2014).
22. Karvonen, L. *et al.* Investigation of second- and third-harmonic generation in few-layer gallium selenide by multiphoton microscopy. *Sci.Rep.* **5,** 10334 (2015).
23. Liu, Z. B., Zhang, X. L., Yan, X. Q., Chen, Y. S. & Tian, J. G. Nonlinear optical properties of graphene-based materials. *Chin. Sci. Bull.* **57,** 2971 (2012).
24. Wang, R. *et al.* Third-harmonic generation in ultrathin films of MoS_2. *ACS Appl. Mater. Interfaces* **6**, 314–318 (2014).
25. Zhang, Y. X. *et al.* Atomic-layer molybdenum sulfide optical modulator for visible coherent light. *Sci. Rep.* **5,** 11342 (2015).

26. Zeng, H. L. *et al.* Optical signature of symmetry variations and spin-valley coupling in atomically thin tungsten dichalcogenides. *Sci. Rep.* **3,** 1608 (2013).
27. Zhou, Y. *et al.* Tuning the dispersion relation of a plasmonic waveguide via graphene contact. *Europhys. Lett.* **107,** 34007 (2014).
28. Zhou, K. G. *et al.* Size-dependent nonlinear optical properties of atomically thin transition metal dichalcogenide nanosheets. *Small*, **11,** 694–701 (2015).
29. Chen, B. G. *et al.* Graphene coated ZnO nanowire optical waveguides. *Opt. Express* **22,** 24276 (2014).
30. Zhang, L. M. *et al.* Three-dimensional spirals of atomic layered MoS_2. *Nano Lett.* **14,** 6418–6423 (2014).
31. Wang, K. P. *et al.* Broadband ultrafast nonlinear absorption and nonlinear refraction of layered molybdenum dichalcogenide semiconductors. *Nanoscale*, **6,** 10530–10535 (2014).
32. Xia, F. N., Wang, H., Xiao, D., Dubey, M. & Ramasubramaniam, A. Two-dimensional material nanophotonics. *Nat. Photonics* **8,** 899–907 (2014).
33. Zhang, H. *et al.* Molybdenum disulfide (MoS_2) as a broadband saturable absorber for ultra-fast photonics. *Opt. Express* **22,** 7249–7260 (2014).
34. Yin, Y., Cheng, Z. G., Wang, L., Jin, K. J. & Wang, W. L. Graphene, a material for high temperature devices–intrinsic carrier density, carrier drift velocity, and lattice energy. *Sci. Rep*. **4,** 5758 (2014).
35. Tian, Y. C. *et al.* Coherent generation of photo-thermo-acoustic wave from graphene sheets. *Sci. Rep*. **5,** 10582 (2015).
36. Prineas, J. P., Johnston, W. J., Yildirim, M., Zhao, J. & Smirl, L. Tunable slow light in Bragg-spaced quantum wells. *Appl. Phys. Lett.* **89,** 241106 (2006).
37. Dawes, A. M. C., Illing, L., Clark, S. M. & Gauthier, D. J. All-optical switching in rubidium vapor. *Science* **308,** 672–674 (2005).
38. Han, X. F. *et al.* Single-photon level ultrafast all-optical switching. *Appl. Phys. Lett.* **92,** 151109 (2008).
39. Wang, B. L. *et al.* Second-harmonic generation from metallic nanohole arrays. *Sci. Rep*. **3,** 2358 (2013).
40. Kumar, N. *et al.* Third harmonic generation in graphene and few-layer graphite films. *Phys. Rev. B* **87,** 121406 (R) (2013).
41. Hendry, E., Hale, P. J., Moger, J. & Savchenko, A. K. Coherent nonlinear optical response of graphene. *Phys. Rev. Lett.* **105,** 097401 (2010).
42. Sun, F. *et al.* Double charge ordering states and spin ordering state observed in a RFe_2O_4 system. *Sci. Rep*. **4,** 6429 (2014).
43. Shi, B. X. *et al.* Broadband ultrafast spatial self-phase modulation for topological insulator Bi_2Te_3 dispersions. *Appl. Phys. Lett.* **107,** 151101 (2015).
44. Durbin, S. D., Arakelian, S. M. & Shen, Y. R. Laser-induced diffraction rings from a nematic-liquid-crystal film. *Opt. Lett.* **6,** 411–413 (1981).
45. Ji, W., Chen, W. Z., Lim, S. H., Lim, J. Y. & Guo, Z. X. Gravitation-dependent, thermally-induced self-diffraction in carbon nanotube solutions. *Opt. Express* **14,** 8958–8966 (2006).
46. Pouzet, J., Bernede, J. C. & Ouadah, A. Optical and electrical properties of textured $MoSe_2$ layers obtained by annealing Mo and Te thin films under Se pressure. *Phys. Stat. Sol. (a)* **139,** 471 (1993).

Acknowledgements

This work was supported by the National Basic Research Program of China (Grant No. 2012CB821402), the National Nature Science Foundation of China (Grant No. 11574383, 11204234 and 11274372), "the Fundamental Research Funds for the Central Universities" of China (Grant No. xjj2012005), and the External Cooperation Program of Chinese Academy of Sciences (Grant No. GJHZ1403).

Author Contributions

J.Z. conceived the idea. W.W., Y.W. and Q.W. conducted the experiment. W.W., Y.W., J.H. and J.Z. analyzed the data. W.W., Y.W. and J.Z. wrote the paper.

Additional Information

Supplementary information accompanies this paper at http://www.nature.com/srep

Competing financial interests: The authors declare no competing financial interests.

How to cite this article: Wang, W. *et al.* Coherent Nonlinear Optical Response Spatial Self-Phase Modulation in $MoSe_2$ Nano-Sheets. *Sci. Rep.* **6**, 22072; doi: 10.1038/srep22072 (2016).